Conference paper

Rayan Zaiter, Mohammad Kassem, Daniele Fontanari, Arnaud Cuisset, Chris J. Benmore and Eugene Bychkov*

Ionic transport and atomic structure of AgI-HgS-GeS_2 glasses

https://doi.org/10.1515/pac-2019-0103

Abstract: *Quasi*-ternary $(AgI)_x(HgS)_{0.5-x/2}(GeS_2)_{0.5-x/2}$ glasses, $10^{-4} \le x \le 0.6$ were studied over a wide composition range covering nearly 4 orders of magnitude in the mobile cation content. The glasses show a remarkable increase of the ionic conductivity by 12 orders of magnitude and exhibit two drastically different ion transport regimes: (i) a power-law critical percolation at $x \lesssim 0.04$, and (ii) a modifier-controlled conductivity, exponentially dependent on $x \gtrsim 0.1$. Using Raman spectroscopy and high-energy X-ray diffraction supported by DFT modelling of the Raman spectra we show that the glass network is essentially formed by corner-sharing CS-$GeS_{4/2}$ tetrahedra. Mercury sulfide in glasses is dimorphic. The majority of Hg species (70 % at $x < 0.2$) exist as two-fold coordinated $(HgS_{2/2})_n$ chains. Silver species have mixed (2I + 2S) tetrahedral environment forming either edge–sharing ES-$Ag_2I_2S_{4/2}$ dimers or corner-sharing $(CS\text{-}AgI_{2/2}S_{2/2})_n$ chains. The relationship between the ionic transport and atomic structure of the glasses is discussed.

Keywords: critical percolation; DFT; diffraction; HgS dimorphism; mixed tetrahedral silver environment; Raman spectroscopy; SSC-2018.

Introduction

Silver halide containing chalcogenide glasses have been intensively investigated over the last few decades owing to their high Ag^+ ionic conductivity [1–3] and a large number of applications in different fields (chemical sensing [4, 5], lithography [6, 7], phase-change memories and related phenomena [8–10], etc.). They are also interesting model systems to investigate the structural role of silver halides in fast ion conducting glasses. A largely accepted approach consists to consider silver halides as dopant salts providing the conductivity enhancement through the expansion of the glass-forming units [11, 12] and neglecting possible chemical interactions between silver halide and a vitreous host. Widely investigated chalcohalide or oxyhalide *quasi*-ternary systems AgY-Ag_2X-M_nX_m, where Y=Cl, Br, I; X=O, S, Se, Te; M=B, Si, P, As, Ge, Sb, Mo, usually contain silver oxide or silver chalcogenide Ag_2X making difficult to study the silver local environment in glasses related to AgY. Only a limited number of papers were devoted either to *quasi*-binary systems AgY-M_2X_3 or *quasi*-ternary vitreous alloys without Ag_2X [13–16].

Mercury chalcogenide glasses seem to be promising materials particularly in the field of optics [17]. Crystalline mercury sulfide exists in two drastically different polymorphic forms in different domains of the

Article note: A collection of invited papers based on presentations at the 13th International Conference on Solid State Chemistry (SSC-2018), Pardubice, Czech Republic, September 16–21, 2018.

***Corresponding author: Eugene Bychkov,** Université du Littoral Côte d'Opale, LPCA, 189A Avenue Maurice Schumann, 59140 Dunkerque, France, e-mail: Eugene.Bychkov@univ-littoral.fr

Rayan Zaiter, Mohammad Kassem, Daniele Fontanari and Arnaud Cuisset: Université du Littoral Côte d'Opale, LPCA, 189A Avenue Maurice Schumann, 59140 Dunkerque, France

Chris J. Benmore: X-ray Science Division, Argonne National Laboratory, Advanced Photon Source, Argonne, IL 60439, USA

P,T-diagram: red chain-like insulator α-HgS (E_g≈2.1 eV), stable below 344 °C, and black tetrahedral narrow-band semiconductor β-HgS (E_g≈0.4 eV), stable at higher temperatures. Diffraction and Raman measurements of glassy mercury thioarsenates HgS-As_2S_3 [17, 18] show that these two mercury bonding patterns are present simultaneously in the glasses. The population and interconnectivity of chain-like and tetrahedral mercury forms determine both the structural features and fundamental glass properties. In other words, the two-fold and four-fold coordinated mercury species act as network former and modifier, respectively.

The main purpose of this work is to study electrical and structural properties of *quasi*-ternary AgI-HgS-GeS_2 glassy system. Introducing silver iodide into mercury thiogermanate vitreous host, one expects to generate and increase the Ag^+ ionic conductivity, important for various applications of these glasses. Using a melt quenching method we were able to produce $(AgI)_x(HgS)_{0.5-x/2}(GeS_2)_{0.5-x/2}$ glasses, containing up to 60 mol.% AgI [19]. The aim of the present paper is (I) to study the ion transport properties using conductivity measurements, (II) to unveil the glass structural features using Raman spectroscopy and high-energy X-ray diffraction experiments combined with DFT modelling of the Raman spectra, and finally (III) to discuss the relationship between the ionic conduction and atomic glass structure.

Experimental

Glass preparation

The $(AgI)_x(HgS)_{0.5-x/2}(GeS_2)_{0.5-x/2}$ glasses were prepared from silver iodide, mercury sulfide, and germanium disulfide precursors via conventional synthesis. The various components in required proportions were sealed under vacuum (10^{-6} mbar) in silica tubes, heated up to 995 °C and homogenised in a furnace. Finally, the melt was quenched in icy salt water.

Conductivity measurements

The alternating current a.c. electrical conductivity of the samples was measured using a Hewlett Packard 4191A impedance meter. The impedance modulus Z and the phase angle θ were obtained in the frequency range 100 Hz to 15 MHz from room temperature up to 170 °C. The direct current d.c. electrical conductivity was measured using a Hewlett Packard 4339B high resistance meter with an applied voltage of 100 volts in the temperature range between 60 and 170 °C depending on the sample composition. Further experimental details are published elsewhere [20].

Raman spectroscopy measurements

Raman spectra were collected at room temperature using a LabRam HR spectrometer (Jobin Yvon Horiba Group) equipped with a triple monochromator, liquid nitrogen cooled CCD detector and a microscope. Raman scattering was excited by a 785 nm solid-state laser and recorded in the 80–850 cm^{-1} spectral range. To avoid crystallisation of the glassy samples, the laser power was set to 1.5 mW and the acquisition time was 300 s. Two to three spectra were registered for each sample at different positions to verify the sample homogeneity and the absence of photo-induced phenomena. The spectrometer resolution was 1 cm^{-1}.

Diffraction measurements

High-energy X-ray diffraction measurements were conducted at the 6-ID-D beamline of the Advanced Photon Source (Argonne National Laboratory, USA). The X-ray energy was 100 keV, providing data at Q values up

to 30 $Å^{-1}$. A 2D setup was used for data collection with a Perkin Elmer model 1621 X-ray area detector. The two-dimensional diffraction patterns were reduced using the Fit2D software [21]. The measured background intensity was subtracted, and corrections were made for the different detector geometries and efficiencies, sample self-attenuation, and Compton-scattering using standard procedures [22] giving the X-ray total structure factor $S_X(Q)$.

DFT modelling

The DFT calculations have been carried out using Gaussian 16 software [23] associated with its graphical user interface GaussView. In order to find a compromise between the cost of the calculations and the accuracy of the results, structural optimisation and harmonic vibrational frequency calculations were performed for size-limited clusters. The DFT calculations were carried out with the Becke [24] three parameters hybrid exchange functional and the Lee–Yang–Parr correlation functional (B3LYP) [25]. The small-core relativistic pseudo-potential basis set (cc-pVTZ-PP) [26] and the effective core potentials available in the Environment Molecular Science Library [27] were employed for cluster geometry optimisation and Raman intensity calculations. All the structures were optimised using the tight convergence option ensuring adequate convergence and reliability of computed wave numbers.

Results and discussion

Ionic conductivity

Typical temperature dependences of the total conductivity for AgI-HgS-GeS_2 glasses are shown in Fig. 1. The electrical conductivity, determined either by the complex impedance method ($\sigma \geq 10^{-8}$ S · cm^{-1}) or from the d.c. measurements ($\sigma < 10^{-8}$ S cm^{-1}) do not show any significant hysteresis effects and obey the Arrhenius law:

$$\sigma = \frac{\sigma_0}{T} \exp\left(-\frac{E_a}{kT}\right), \tag{1}$$

where σ_0 is the pre-exponential factor, E_a the activation energy, k the Boltzmann constant and T the temperature. The room-temperature conductivity σ_{298}, E_a and σ_0 were calculated from a least square fit of the data using Eq. (1) and shown in Figs. 2 and 3.

The room temperature conductivity increases by ≈12 orders of magnitude from 4.5×10^{-15} S · cm^{-1} to 2.0×10^{-3} S · cm^{-1} over 4 orders of magnitude in the silver content y, between $y_{min} = 40$ ppm Ag ($x = 10^{-4}$) and $y_{max} = 27.3$ at.% Ag ($x = 0.6$). Similar conductivity evolution was found for several families of Ag^+ ion conducting sulfide glasses [28–31]. Complementary ^{108m}Ag or ^{110m}Ag tracer diffusion measurements have also revealed a predominantly ionic transport even for extremely diluted glasses when the silver ion transport number was found to be $t_{Ag^+} \approx 1$ for $y \geq 500$ ppm Ag [28, 29, 32].

The conductivity isotherms, Fig. 2, show four different concentration regions: (A) $y \leq 1$–2 at.% Ag ($x \leq 0.02$–0.04), (B) $5 < y \leq 12$ at.% Ag ($0.1 < x \leq 0.3$), (C) $12 < y \leq 22$ at.% Ag ($0.3 < x \leq 0.5$), and (D) $y > 22$ at.% Ag ($x > 0.5$). The detailed description of the ionic conductivity regimes will be given below. The conductivity increase is accompanied by a simultaneous decrease of the conductivity activation energy from 0.96 eV to 0.23 eV, Fig. 3a while the conductivity pre-exponential factor monotonically increases from $\sigma_0 = 4 \times 10^4$ S · cm^{-1} · K to 1×10^6 S · cm^{-1} · K before a sudden drop by 2 orders of magnitude for the region D glasses ($x > 0.5$), Fig. 3b. These vitreous alloys at the limit of the glass-forming range have nearly identical conductivity parameters and contain nanocrystals of silver iodide, identified by the β→α–AgI phase transition at the DSC traces. In the following discussion, the analysis of region D glasses will be omitted.

The observed ionic conductivity evolution in the AgI-HgS-GeS_2 glasses shows characteristic transport regimes for ion-conducting chalcogenide glasses over a wide composition range: (i) critical percolation

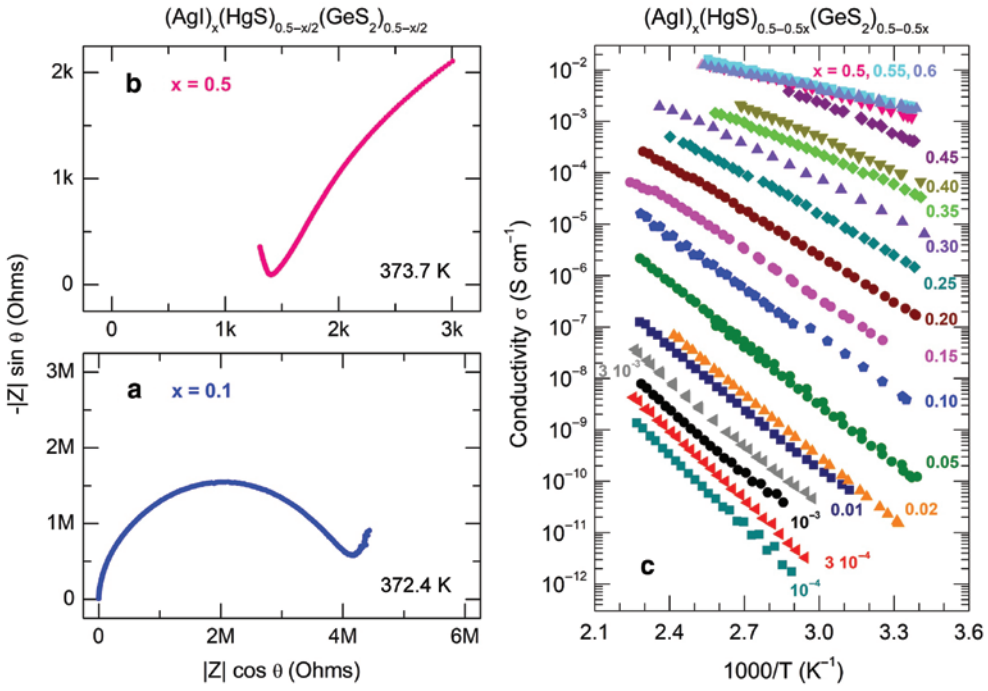

Fig. 1: Electrical characteristics of (AgI)$_x$(HgS)$_{0.5-x/2}$(GeS$_2$)$_{0.5-x/2}$ glasses: typical complex impedance plots of (a) the $x = 0.10$ and (b) the $x = 0.50$ samples at 372.4 K and 373.7 K, respectively; (c) temperature dependences of the total electrical conductivity σ for the entire pseudo-ternary glass system. The numbers indicate the AgI molar fraction x.

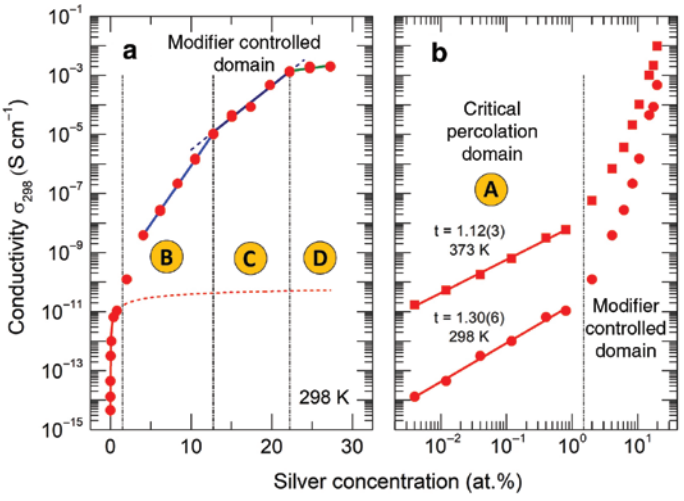

Fig. 2: (a) Room-temperature conductivity of AgI-HgS-GeS$_2$ glasses plotted on a semi-logarithmic scale, and (b) conductivity isotherms of silver iodide mercury thiogermanate glasses at (●, solid circles) 298 K and (■, solid squares) 373 K plotted on a log-log scale. The red solid lines represent a least-square fit of the experimental data points in the critical percolation domain A to Eq. (2); the red dashed line shows a hypothetical critical percolation conductivity beyond the domain A; the solid lines in the modifier-controlled domains B, C and D are drawn as a guide to the eye.

regime for diluted glasses (region A), and (ii) modifier-controlled regime for intermediate- and high Ag-rich vitreous alloys (regions B and C). The main difference compared to previously reported conductivity and tracer diffusion results [28, 29] appears to be two sub-regions B and C for the modifier-controlled domain clearly seen in Fig. 2a by changing the slope $\partial \log \sigma / \partial y$.

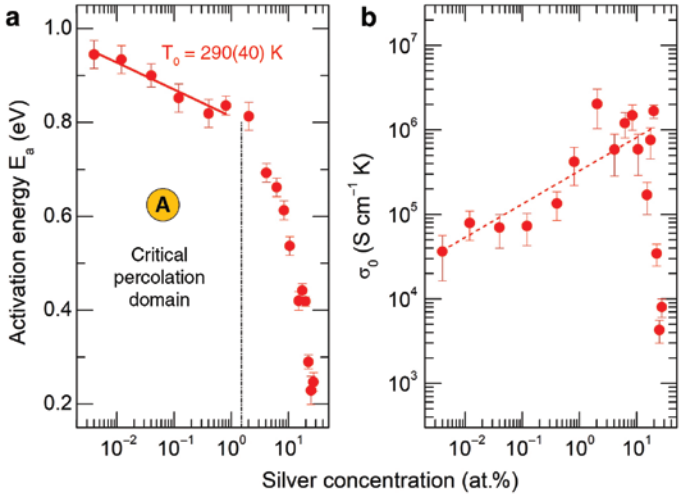

Fig. 3: (a) Conductivity activation energy E_a and (b) conductivity pre-exponential factor σ_0 over a wide composition range in AgI-HgS-GeS$_2$ glasses. The solid line represents a least-square fit of the E_a experimental data points in the critical percolation domain A to Eq. (4). The dashed line is drawn as a guide to the eye.

Critical percolation domain A ($y_c < y \leq 1$–2 at.% Ag)

The ionic conductivity evolution in region A exhibit all characteristic features of the critical percolation regime [32]. Extremely diluted $(AgI)_x(HgS)_{0.5-x/2}(GeS_2)_{0.5-x/2}$ chalcogenide glasses show a rapid increase of conductivity (≈3 orders of magnitude) in a limited concentration range, 40 ppm $\leq y \lesssim$ 1–2 at.% Ag (region A), revealing a power-law composition dependence, Fig. 2b:

$$\sigma_i(y, T) = \sigma_i(1, T) y^{t(T)}, \tag{2}$$

where $\sigma_i(1, T)$ is the ionic conductivity of a hypothetical percolation-controlled phase at $y = 1$, and $t(T)$ is the temperature dependent power-law exponent

$$t(T) = t_0 + T_0 / T, \tag{3}$$

where t_0 is the critical exponent at $T = \infty$ and T_0 is the critical fictive temperature which reflects the interconnectivity of an infinite percolation cluster.

The conductivity activation energy in the critical percolation domain, $E(y)$, is also dependent on T_0

$$E(y) = E_0 - kT_0 \ln(y / y_c), \tag{4}$$

where E_0 is the activation energy at the percolation threshold $y_c \cong 30$ ppm Ag [32] and $kT_0 \ln(y/y_c)$ is the configuration entropy term related to the infinite percolation cluster(s) frozen below T_g. The derived critical temperature $T_0 = 273 \pm 9$ K, determined from the conductivity isotherms plotted on a log-log scale, Fig. 2b, appears to be consistent with that calculated using Eq. (4), $T_0 = 290 \pm 40$ K, Fig. 3a.

The structural hypothesis behind the critical percolation regime suggests a random distribution of silver sites within the glass network [32]. The average Ag–Ag separation distance, calculated using a Wigner–Seitz type relation, $r_{Ag-Ag} \propto \sqrt[3]{V_a N_a^{-1} y^{-1}}$, where V_a is the glass molar volume and N_a the Avogadro constant, changes between 80 Å and 10 Å depending on the silver content y. Consequently, the preferential conduction pathways are not yet formed in the critical percolation domain A.

Modifier-controlled regions B and C

The ionic conductivity of the $(AgI)_x(HgS)_{0.5-x/2}(GeS_2)_{0.5-x/2}$ glasses diverges from the power-law behavior (2) in the modifier-controlled domain at higher silver content $y > 5$ at.% Ag ($x > 0.1$), Fig. 2. Instead, one observes an exponential increase of conductivity as a function of y:

$$\sigma_i(y) = \sigma_i(0)\exp(ay), \tag{5}$$

where a is a constant. Pulsed neutron and hard X-ray diffraction as well as small-angle neutron scattering experiments reveal a non-random silver distribution in the modifier-controlled domain and formation of preferential conduction pathways formed by direct contacts of corner- and/or edge-sharing silver-related coordination polyhedra [33–35]. We should however note a remarkable change in the slope $\partial \log \sigma / \partial y$ by a factor of 2 at $y \approx 12$ at.% Ag ($x \approx 0.3$) assuming some structural changes between regions B and C. Raman spectroscopy and high-energy X-ray diffraction were used to unveil possible differences in the local and intermediate-range order of AgI-HgS-GeS_2 glasses.

Raman spectra

Vitreous matrix $(HgS)_{0.5}(GeS_2)_{0.5}$

The Raman spectra of glassy $(HgS)_{0.5}(GeS_2)_{0.5}$ and GeS_2 are shown in Fig. 4b, normalised to the A_1 in-phase breathing mode of corner-sharing CS-$GeS_{4/2}$ tetrahedra at 340 cm^{-1}, Fig. 4c. The equimolar mercury thioger-

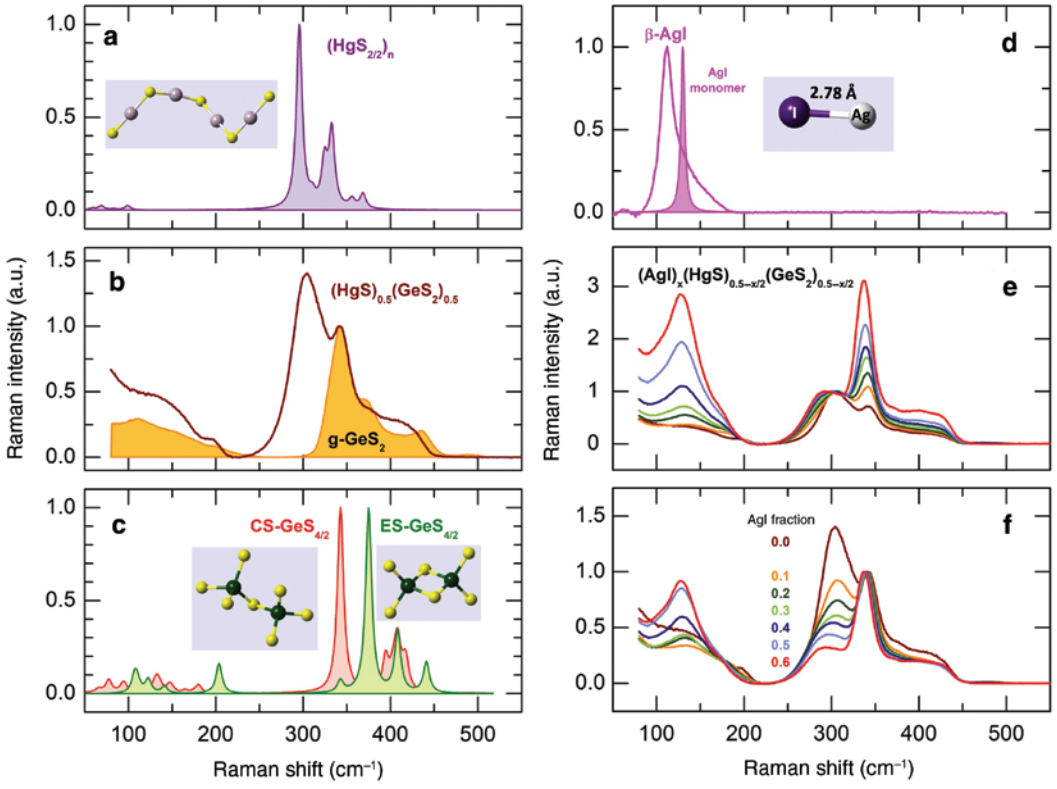

Fig. 4: Experimental and DFT Raman spectra related to AgI-HgS-GeS_2 glasses: (a) DFT chain-like cluster Hg_4S_5 [17], (b) equimolar glassy host $(HgS)_{0.5}(GeS_2)_{0.5}$ and glassy GeS_2, (c) corner- and edge-sharing CS-Ge_2S_7 and ES-Ge_2S_6 clusters [38], (d) hexagonal β-AgI and DFT monomer AgI, selected $(AgI)_x(HgS)_{0.5-x/2}(GeS_2)_{0.5-x/2}$ glasses normalised to (e) the Hg-S symmetric stretching mode at 300 cm^{-1}, or to (f) the Ge-S breathing mode in CS-$GeS_{4/2}$ tetrahedra at 340 cm^{-1}.

manate glass is characterised by the most intense A_1 symmetric Hg-S stretching feature at 300 cm^{-1} similar to that in mercury thioarsenate glasses $(HgS)_x(As_2S_3)_{1-x}$ [17]. The DFT simulations have revealed the origin of the 300 cm^{-1} mode to be related to $(HgS_{2/2})_n$ chains, Fig. 4a, with rather weak interchain interactions in contrast to trigonal cinnabar α-HgS [36, 37]. Similar situation seems to exist in glassy $(HgS)_{0.5}(GeS_2)_{0.5}$. Mercury sulfide alloying with g-GeS_2 reduces substantially the population of edge-sharing ES-$GeS_{4/2}$ tetrahedra evidenced by a decreasing intensity of the A_1^c companion mode at 370 cm^{-1} and F_2 asymmetric stretching mode at 435 cm^{-1}, Fig. 4b,c. In addition, a small red-shift, –1.5 cm^{-1}, was observed for the A_1 in-phase Ge-S breathing in CS-$GeS_{4/2}$ at ≈340 cm^{-1}. The Raman spectroscopy was however unable to distinguish between the two- and four-fold coordinated mercury species in sulfide glasses [17, 18]. Mercury sulfide dimorphism in the equimolar vitreous host and *quasi*-ternary AgI-HgS-GeS_2 glasses will be discussed on the basis of diffraction studies.

Vibration modes in AgI-HgS-GeS_2 glasses

Alloying with AgI changes dramatically the Raman spectra, Fig. 4e,f. As expected, the relative intensity of the A_1 symmetric Hg-S stretching mode at 300 cm^{-1} decreases while a new low-frequency feature at ≈140 cm^{-1} emerges and grows with increasing silver iodide content x simultaneously with the A_1 in-phase Ge-S breathing in CS-$GeS_{4/2}$ units at 340 cm^{-1}. The 300 cm^{-1} Hg-S stretching shows a low-frequency side broadening assuming the appearance of an additional mode at 270 cm^{-1} increasing in intensity with x. The emerging 140 cm^{-1} feature is similar to that in hexagonal β-AgI, corresponding to the Ag-I stretching, Fig. 4d. The DFT modelling of a simple AgI monomer confirms this assignment. We should also note a systematic red shift of the 340 cm^{-1} Ge-S breathing in CS-$GeS_{4/2}$ tetrahedra with increasing x, clearly seen in Fig. 4f, and further decrease in intensity of high-frequency Ge-S stretching modes, $\nu \geq 370$ cm^{-1}, corresponding to ES-$GeS_{4/2}$ entities.

Subtraction of the scaled Raman spectral envelope for vitreous host $(HgS)_{0.5}(GeS_2)_{0.5}$ from the spectra of AgI-HgS-GeS_2 glasses[1] and data analysis of the entire and difference Raman spectra allows complementary structural information to be obtained. It should, however, be noted that the difference spectra assume the subtraction of HgS-GeS_2 related vibrations, e.g. Ge-S and Hg-S stretching and bending/deformation modes. The remaining vibrations should be related to AgI-based structural units and vibrational (structural) differences between the subtracted host, $(HgS)_{0.5}(GeS_2)_{0.5}$, and *quasi*-ternary glasses changing with increasing silver iodide content.

The difference spectra, Fig. 5a, confirm a simultaneous growth of three vibration features with increasing x: (1) the Ag-I stretching at 140 cm^{-1}, (2) a new 270 cm^{-1} mode, and (3) the A_1 in-phase Ge-S stretching at 340 cm^{-1}, already seen before subtraction in Fig. 4e. The asymmetric peak at ≈270 cm^{-1} seems to be related to symmetric and asymmetric Ag-S stretching, indicating a mixed silver environment (I + S) in the *quasi*-ternary glasses. The DFT modelling of the Ag_2S triatomic cluster, Fig. 5b, is consistent with this assumption for rather short Ag-S interatomic distances of 2.43 Å. The Raman spectrum of monoclinic β-Ag_2S, also shown in Fig. 5b, is shifted to lower frequencies since the Ag-S first neighbour distances in crystalline silver sulfide are longer and spread over a wide range, 2.49 Å ≤ $r_{Ag\text{-}S}$ ≤ 2.69 Å [40].

The 140 cm^{-1} spectral feature is, at least, bimodal; one observes a high-frequency shoulder at ≈180 cm^{-1}, whose relative intensity and position depends on x. The nature of this shoulder is not yet clear, although hexagonal β-AgI also exhibits asymmetric Ag-I stretching feature with high-frequency shoulder, Fig. 4d.

The Ge-S stretching frequencies between 300 and 450 cm^{-1} are most difficult to discuss since they, in principle, should be subtracted. However, the A_1 in-phase Ge-S breathing at ≈340 cm^{-1} increases almost simultaneously with the Ag-I stretching at ≈140 cm^{-1}. It could be related to the fact that the mixed silver environment and additional Ge-S stretching modes are connected. They would appear simultaneously

1 The difference spectra after the subtraction procedure, $I(x, \nu) - k \times I(0, \nu)$, where $I(x, \nu)$ and $I(0, \nu)$ are the spectral envelopes for *quasi*-ternary glasses and vitreous host, respectively, were divided by the constant k, i.e. normalised to the constant spectral envelope of the glassy matrix.

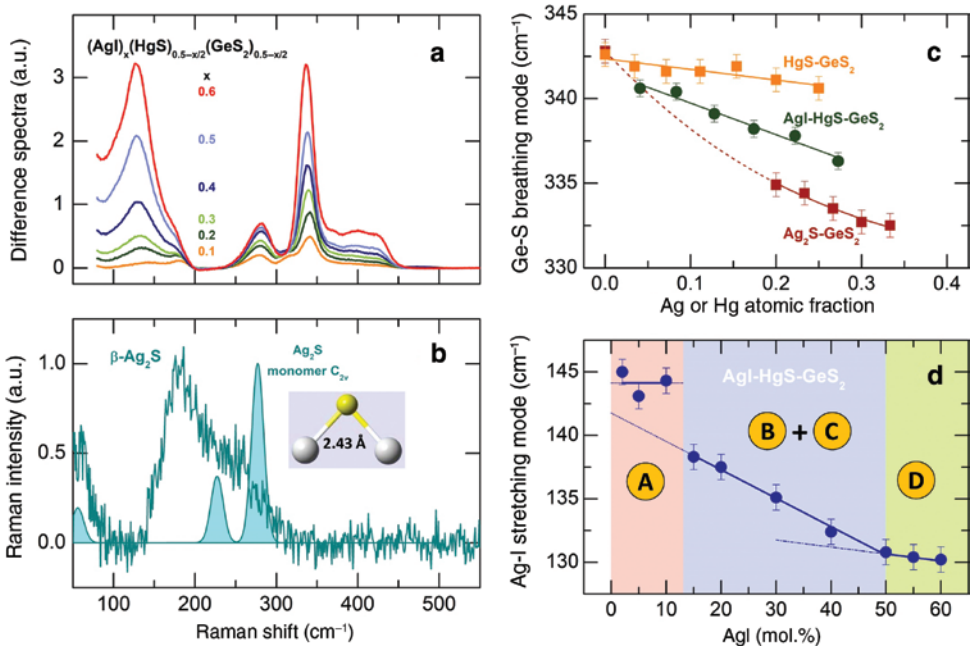

Fig. 5: Difference Raman spectra and derived fitting parameters for AgI-HgS-GeS$_2$ glasses: (a) the difference spectra for selected glasses obtained by subtraction of the scaled spectral envelope for glassy host (HgS)$_{0.5}$(GeS$_2$)$_{0.5}$; the indicated numbers correspond to the AgI fraction in the glass; (b) the experimental and DFT Raman spectra of β-Ag$_2$S and Ag$_2$S triatomic cluster of C_{2v} symmetry; (c) the position of the A_1 in-phase breathing mode of CS-GeS$_{4/2}$ tetrahedra in HgS-GeS$_2$ [19], AgI-HgS-GeS$_2$ (this work) and Ag$_2$S-GeS$_2$ [39] glasses; (d) the position of the Ag-I stretching mode in AgI-HgS-GeS$_2$ glasses as a function of the AgI content.

when silver iodide is dispersed at the molecular level in the host network approaching CS-GeS$_{4/2}$ tetrahedra and completing the existing Ag-I bonds by Ag-S-Ge linkages. The high-frequency Ge-S stretching (>340 cm^{-1}) includes the F_2 asymmetric vibrations of CS-GeS$_{4/2}$ tetrahedra and probably yield some indications of CS-Ge$_2$S$_7$ dimers at ≈400 cm^{-1}, observed previously in silver thiogermanate glasses [39, 41]. The red shift of the A_1 in-phase Ge-S breathing mode in HgS-GeS$_2$ [19], AgI-HgS-GeS$_2$ (this work) and Ag$_2$S-GeS$_2$ [39] glass families, Fig. 5c, is also consistent with iodine/sulfur mixed silver environment. As mentioned above, the HgS-GeS$_2$ *quasi*-binary system shows a weak red shift, $-(6.3 \pm 1.4)$ cm^{-1} mol^{-1}, since the mercury sulfide chains $(HgS_{2/2})_n$ are rather network-forming entities than network modifiers. Silver thiogermanate glasses Ag$_2$S-GeS$_2$ show a typical modifier effect when formation of non-bridging sulfur and network fragmentation lead to a strong red shift for homogeneous Ag-rich glasses ($y \gtrsim 20$ at.% Ag), $-(20 \pm 2)$ cm^{-1} mol^{-1}. Similar red shift was observed for the AgI-HgS-GeS$_2$ vitreous alloys, $-(18.6 \pm 1.6)$ cm^{-1} mol^{-1}, emphasising the structural role of silver iodide as modifier through the Ag-S-Ge linkages and network fragmentation evidenced by a significant decrease of the glass transition temperature from 237 °C ($y = 0$) to 165 °C ($y = 27.3$ at.% Ag) [19].

The Ag-I stretching also exhibits characteristic changes with increasing x, Fig. 5d, corresponding to different ion transport regimes in the (AgI)$_x$(HgS)$_{0.5-x/2}$(GeS$_2$)$_{0.5-x/2}$ glasses, composition ranges A, B, C and D. The silver-diluted glasses ($x \lesssim 0.1$, roughly the critical percolation domain A) show high and nearly constant stretching frequencies, 144.1 ± 0.6 cm^{-1}. These values suggest the shortest and invariant Ag-I interatomic distances in the *quasi*-ternary system, which seem to be related to AgI-based isolated structural entities distributed in the host network and experiencing the tectonic contraction imposed by the neighbouring network backbone. Modifier-controlled domains B and C are characterised by a strong red shift, $-(22.4 \pm 1.1)$ cm^{-1} mol^{-1}, presumably indicating the formation and evolution of preferential conduction pathways through the direct contacts of AgI-based coordination polyhedra. The non-homogeneous region D glasses show nearly constant Ag-I stretching frequencies, ≈130 cm^{-1}, in accordance with invariant thermal and conductivity properties.

Nevertheless, neither the Ge-S nor Ag-I stretching has reflected the observed change in the slope $\partial \log \sigma / \partial y$ by a factor of 2 between regions B and C.

High-energy X-ray diffraction

Glassy $(HgS)_{0.5}(GeS_2)_{0.5}$

Typical Faber-Ziman X-ray structure factors $S_x(Q)$ of vitreous mercury thiogermanate matrix and glassy GeS_2 are shown in Fig. 6a.

In contrast to g-GeS_2 revealing typical diffraction pattern for binary germanium sulfide glasses [42–45] with a very intense First Sharp Diffraction Peak (FSDP) at $Q_0 = 1.04$ Å^{-1}, weak Principal Peak (PP) at $Q_1 \approx 2.3$ Å^{-1} followed by a strong third peak at 3.7 Å^{-1}, the $S_x(Q)$ of equimolar mercury thiogermanate is characterised by a significant reduction of the FSDP by a factor of 16, also shifted to higher $Q_0 = 1.17$ Å^{-1}, quite intense PP at $Q_1 \approx 2.1$ Å^{-1}, whose amplitude becomes comparable with that of the third peak, and reduced high-Q oscillations. The PP additionally exhibits a low-Q broadening hiding the second pre-peak at $Q_{0b} \approx 1.7$ Å^{-1} related to Hg–Hg intermediate range order correlations, clearly seen in mercury thioarsenate glasses HgS-As_2S_3 [18]. The observed differences seem to be related to an extensive fragmentation of Ge-S network, confirmed by strongly decreasing glass transition temperatures from ≈500 °C (g-GeS_2) to 237 °C (vitreous mercury thiogermanate), and presumably dramatic changes in the ring population. Mercury sulfide species also seem to filling up a large number of available cavities and voids in the network structure of glassy GeS_2, proved to exist by *ab initio* molecular dynamics AIMD [46, 47]. Basically, alloying with HgS appears to be reminiscent of the effect of high pressure: shrinking and shifting to higher Q the FSDP, growing the PP [48].

The total correlation functions $T_x(r)$ in r-space, derived through the usual Fourier transform using the Lorch window function [49], are shown in Fig. 6b. The Ge-S first neighbour correlations at 2.21 Å in glassy GeS_2 are completed by longer Hg-S contacts in vitreous $(HgS)_{0.5}(GeS_2)_{0.5}$, yielding a broad first peak in $T_x(r)$, highlighted in red in Fig. 6b. The short Ge–Ge second neighbour correlations at 2.9 Å, highlighted in blue in Fig. 6b and corresponding to ES-units in glassy GeS_2, became by a factor of 2 smaller in the mercury thiogermanate host, consistent with qualitative estimation from the Raman data, Fig. 4b. We should also note a nearly flat high-r correlations in $(HgS)_{0.5}(GeS_2)_{0.5}$, filling the gap between the second (at ≈3.5 Å) and more distant neighbours, except for a visible peak at 5.5 Å, in contrast to multiple distinct high-r features in g-GeS_2, related to a pronounced intermediate range order and ring statistics [46, 50, 51].

Fitting the first neighbour peak in $T_x(r)$ with two Gaussians, Fig. 6c, one obtains a tetrahedral Ge-S coordination while the mercury-sulfur local environment appears to be a mixture of two-fold Hg_{2F}-S and four-fold coordinated Hg_{4F}-S species, $N_{Hg\cdot S} = 2.7$. Consequently, a three-peak fitting was necessary with the following constraint on C_{2F}^{Hg} and C_{4F}^{Hg} peak areas [18]:

$$2 - N_{Hg\cdot S}^{2F} = \frac{1}{2} N_{Hg\cdot S}^{4F} = 2 - \frac{r_{2F} C_{2F}^{Hg}}{w_{Hg\cdot S}(Q)} = \frac{1}{2} \frac{r_{4F} C_{4F}^{Hg}}{w_{Hg\cdot S}(Q)}, \tag{6}$$

where $N_{Hg\cdot S}^{2F}$ and $N_{Hg\cdot S}^{4F}$ are the partial coordination numbers, r_{2F} and r_{4F} the positions of the peaks, corresponding to two-fold and four-fold coordinated mercury, and $w_{Hg\cdot S}(Q)$ is the Q-dependent X-ray Hg-S weighting factor. The derived $N_{Hg\cdot S}^{2F}$ and $N_{Hg\cdot S}^{4F}$ partial coordination numbers were used to calculate the fraction of four-fold coordinated mercury species f_{Hg}^{4F}:

$$f_{Hg}^{4F} = \frac{N_{Hg\cdot S}^{4F}}{4} = 1 - \frac{N_{Hg\cdot S}^{2F}}{2}. \tag{7}$$

The calculated f_{Hg}^{4F} fraction, $f_{Hg}^{4F} = 0.33 \pm 0.04$, shows the majority of mercury species in glassy $(HgS)_{0.5}(GeS_2)_{0.5}$ belong to the chain-like fragments $(HgS_{2/2})_n$, similar to that in Hg-rich mercury thioarsenate glasses [18]. The Hg_{2F}-S, $r_{2F} = 2.30$ Å, and Hg_{4F}-S, $r_{4F} = 2.41$ Å, interatomic distances are shorter than those in

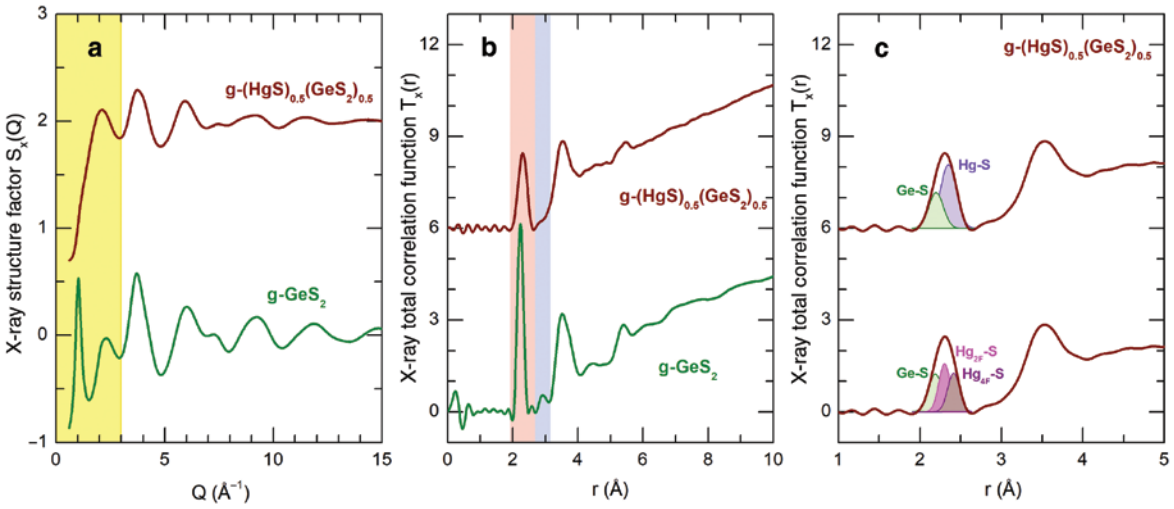

Fig. 6: High-energy X-ray diffraction data for glassy GeS_2 and $(HgS)_{0.5}(GeS_2)_{0.5}$: (a) the structure factors $S_X(Q)$ over a limited Q-range, the First Sharp Diffraction Peak and the Principal Peak are highlighted in yellow; (b) the total correlation functions $T_X(r)$, the first-neighbour correlations are highlighted in light red, the short Ge-Ge second neighbour contacts in light blue; (c) fitting the first neighbour peak in $T_X(r)$ for g-$(HgS)_{0.5}(GeS_2)_{0.5}$ with two (Ge-S and Hg-S) or three (Ge-S, Hg_{2F}-S and Hg_{4F}-S) Gaussians.

the HgS-As_2S_3 system and trigonal chain-like cinnabar α-HgS [52] or cubic metacinnabar β-HgS [53], consisting of $HgS_{4/4}$ tetrahedra, but the difference, $\Delta r = r_{4F} - r_{2F} = 0.11 \pm 0.02$ Å, appears to be coherent both with glassy thioarsenates and crystalline mercury sulfides, 0.09 Å $\leq \Delta r \leq$ 0.16 Å.

Short- and intermediate-range order in AgI-HgS-GeS_2 glasses

The X-ray structure factors $S_X(Q)$ for *quasi*-ternary $(AgI)_x(HgS)_{0.5-x/2}(GeS_2)_{0.5-x/2}$ glasses show a remarkable evolution with increasing AgI content, Fig. 7a. The weak FSDP disappears completely while the PP progressively becomes narrower, mostly because of decreasing mercury concentration and vanishing the hidden Hg–Hg pre-peak at 1.7 Å^{-1}. The PP amplitude changes non-monotonously, increasing up to $x \approx 0.3$ and decreasing with further silver iodide additions. The next two oscillations in the $S_X(Q)$, shown by red arrows in Fig. 7a, exhibit even more surprising behavior. They are strongly shifted to lower Q simultaneously changing the amplitude with a minimum at $x \approx 0.3$. The changing shape of the $S_X(Q)$ reflects structural changes in the *quasi*-ternary glasses. The high-Q oscillations are also shifted to lower Q implying the increase in average interatomic distances.

Likewise, the total correlation functions $T_X(r)$ exhibit a dramatic evolution, Fig. 7b. The unresolved peak at 2.35 Å containing Ge-S and Hg-S first neighbour contacts monotonically decreases with x following the compositional changes. Instead, a new peak at 2.7 Å emerges, grows with x shifting to higher r. The amplitude of this peak becomes predominant at $x \gtrsim 0.2$. The second neighbour peak at 3.5 Å also decreases with x and shifts to higher r. In addition, a new second neighbour feature at 4.4 Å emerges and becomes predominant for AgI-rich glasses, $x > 0.3$. A single visible high-r feature of the vitreous mercury thiogermanate host at 5.5 Å rapidly disappears in the critical percolation domain A. Instead, broad asymmetric correlations emerge at ≈6.6 Å and grow with x.

The five-component AgI-HgS-GeS_2 glasses imply 15 partials. Consequently, the full analysis of the high-r features is impossible without AIMD or related modelling. Nevertheless, we can try to elucidate the local structure of *quasi*-ternary glasses limiting to the first neighbour correlations. The Raman spectroscopy results clearly show the presence of CS-$GeS_{4/2}$ tetrahedra, HgS- and AgI-related structural units. As the first step, a three-peak fitting was carried out imposing a tetrahedral constraint on Ge-S correlations. At low $x < 0.2$, it yields stable Hg-S structural parameters, comparable with those in glassy $(HgS)_{0.5}(GeS_2)_{0.5}$. However, the Ag-I

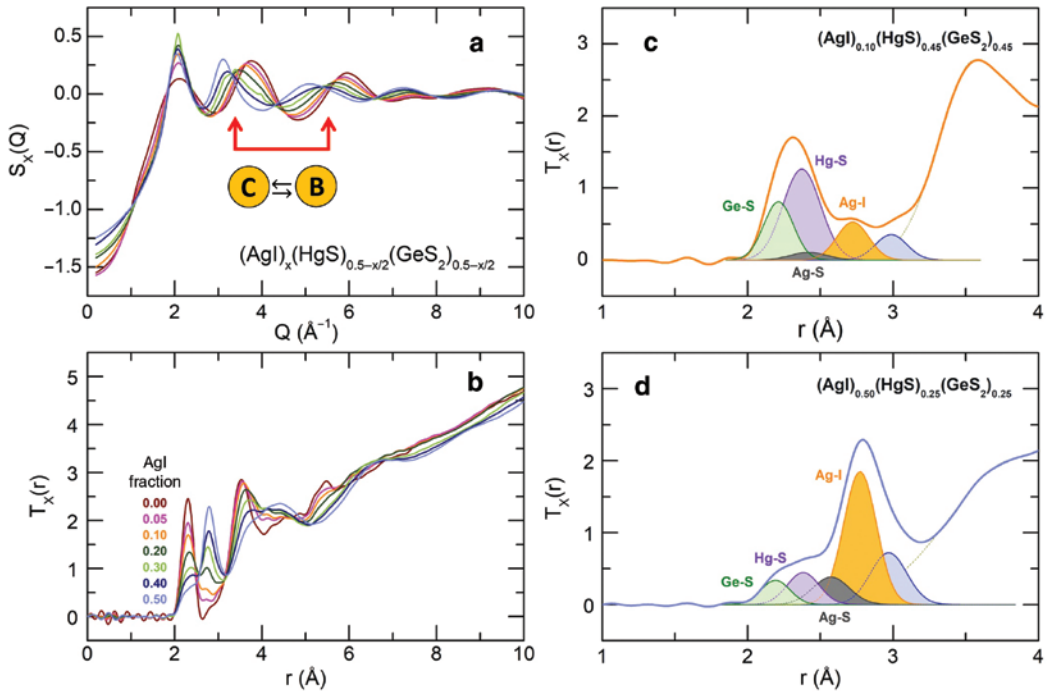

Fig. 7: High-energy X-ray diffraction data for selected AgI-HgS-GeS$_2$ glasses: (a) the structure factors $S_x(Q)$ over a limited Q-range and (b) the total correlation functions $T_x(r)$, colour-coded numbers denote the AgI fraction in glasses. Typical fitting results for (c) (AgI)$_{0.10}$(HgS)$_{0.45}$(GeS$_2$)$_{0.45}$ and (d) (AgI)$_{0.50}$(HgS)$_{0.25}$(GeS$_2$)$_{0.25}$ glasses, the Ge-S, Hg-S, Ag-S, and Ag-I first neighbour correlations are highlighted in green, violet, grey and yellow, respectively, undefined closest second neighbour contacts are depicted in blue. See text for further details.

local coordination over the entire composition range, $0.05 \le x \le 0.50$, was found to be low, $2.5 \le N_{\text{Ag-I}} < 3.0$. As a result, we have excluded a pure iodine environment for silver since the overwhelming majority of Ag-I species in inorganic and metal-organic compounds have a tetrahedral silver coordination. Taking into account the Raman spectroscopy results, the only reasonable alternative appears to be a mixed (I + S) environment frequently observed in silver chalcohalides [54–56] and coordination polymers [57, 58]. Subsequent fittings using the imposed 3:1, 2:2 and 1:3 iodine/sulfur stoichiometry have shown the best results assuming 2I + 2S nearest neighbours around silver. Typical results are shown in Fig 7c,d taking the contrasting compositions, $x = 0.10$ and $x = 0.50$. The derived mixed silver environment shows apparent limitations of the structural models considering only the expansion effects of silver halides in the host network.

The Ag-I interatomic distances are changing significantly with increasing silver iodide content, Fig. 8a. The lowest and invariant values $r_{\text{Ag-I}} = 2.70 \pm 0.01$ Å were found for diluted glasses (the critical percolation domain A). The glasses from the modifier-controlled sub-regions B and C show a monotonic increase of $r_{\text{Ag-I}}$ up to 2.77 ± 0.01 Å. The observed evolution is consistent with the composition dependence of the Ag-I stretching frequencies, Fig. 5d.

The fitting parameters for the Hg-S first neighbour peak were allowed to be completely free. In this particular case, no distinction was made between the two contributions: Hg$_{2F}$-S and Hg$_{4F}$-S. The derived average Hg-S coordination number, shown in Fig. 8b, reveals a step-like decrease within the sub-region B, $x \lesssim 0.3$. As a result, the basic mercury-related structural motif in region C glasses appears to be the chain-like $(HgS_{2/2})_n$ fragments. This change in mercury speciation seems to be the origin of a different slope $\partial \log \sigma / \partial y$ in the modifier-controlled domain at $x \approx 0.3$, Fig. 2a, and also is hidden behind the changing shape of the $S_x(Q)$ for *quasi*-ternary AgI-HgS-GeS$_2$ glasses, Fig. 7a.

The remaining question to solve appears to be a possible structural difference between the critical percolation domain A and modifier-controlled sub-regions B and C. In fact, the ionic conductivity measurements limit the critical percolation regime to $x \lesssim 0.04$, while the modifier-controlled regime starts at $x \gtrsim 0.10$, Figs. 2

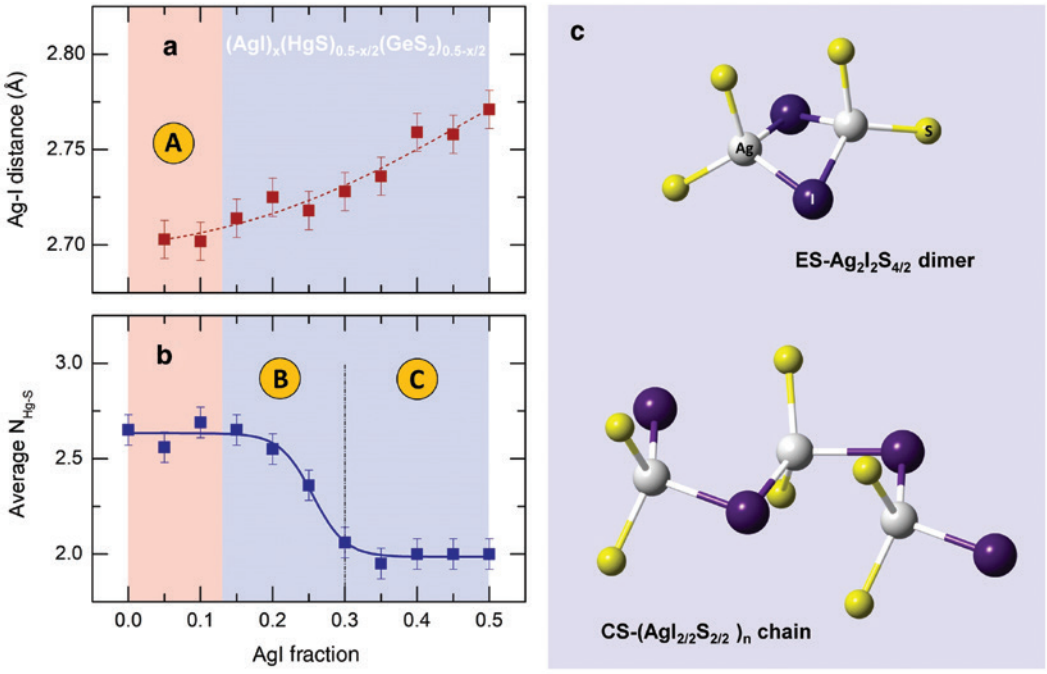

Fig. 8: Selected fitting parameters and suggested structural motifs in $(AgI)_x(HgS)_{0.5-x/2}(GeS_2)_{0.5-x/2}$ glasses: (a) the composition dependence of the Ag-I interatomic distances as a function of x; the critical percolation domain A is characterised by the lowest and invariant Ag-I first neighbour correlations; (b) the average Hg-S local coordination number, the modifier-controlled subdomain C contains essentially the two-fold chain-like mercury species $(HgS_{2/2})_n$; (c) schematic representation of edge-sharing ES-$Ag_2I_2S_{4/2}$ dimers and corner-sharing chain-like fragments (CS-$AgI_{2/2}S_{2/2})_n$ supposed to be the predominant silver-containing entities in diluted (region A) and Ag-rich glasses (regions B and C).

and 3. The grey region in between, $0.04 \lesssim x \lesssim 0.10$, structurally behaves as the critical percolation domain but shows an intermediate behaviour between the two ion transport regimes.

The tetrahedral mixed (2I + 2S) silver environment can be realised using two contrasting approaches: (a) isolated edge-sharing ES-$Ag_2I_2S_{4/2}$ dimers, and (b) extended corner-sharing chain-like fragments (CS-$AgI_{2/2}S_{2/2})_n$, Fig. 8c. We believe the ES-dimers exist in the critical percolation domain A while the CS-chains are characteristic of the modifier-controlled sub-regions B and C, forming the preferential conduction pathways. Both entities have crystalline analogues [54–58] and satisfy the requirements of the critical percolation regime (isolated randomly distributed ES-dimers in the glass network) or modifier-controlled regime (extended mixed CS-chains ensuring high ionic mobility of Ag^+ cations through the pathways with the presence of large polarisable anions).

A possible answer would include the count of Ag–Ag correlations. In the ES-$Ag_2I_2S_{4/2}$ dimers, the short Ag–Ag distances occur at 3.1–3.3 Å [55, 57] and $N_{Ag-Ag} = 1$. In the $(CS\text{-}AgI_{2/2}S_{2/2})_n$ chains, the Ag–Ag correlations are longer, 4.0 Å $\leq r_{Ag-Ag} \leq$ 4.5 Å [59, 60] and $N_{Ag-Ag} = 2$. The total correlation functions show a short second neighbour peak at ≈3 Å, highlighted in blue in Fig. 7c,d. However, the origin of this peak cannot be identified in a 5-component glass. Except short Ag–Ag correlations, similar interatomic distances can possibly provide Hg-Ag or Hg–Hg atomic pairs [59, 60]. Extensive AIMD modelling would be necessary to solve this question.

Conclusions

Quasi-ternary $(AgI)_x(HgS)_{0.5-x/2}(GeS_2)_{0.5-x/2}$ glasses, $10^{-4} \leq x \leq 0.6$, studied over a wide composition range covering nearly 4 orders of magnitude in the mobile cation content y, show a remarkable increase of the ionic

conductivity of ≈12 orders of magnitude and exhibit two drastically different ion transport regimes: (i) a power-law critical percolation (region A, $x \lesssim 0.04$), and (ii) a modifier-controlled conductivity, exponentially dependent on $x \gtrsim 0.1$. The homogeneous glasses in the modifier-controlled domain ($0.1 \lesssim x \lesssim 0.5$) can be subdivided into regions B and C with a threshold concentration $x \approx 0.3$ based on the slope $\log \sigma / \partial y$, which differs by a factor of 2 in the two subdomains. Glasses at the limit of the glass-forming range (region D, $x \gtrsim 0.5$) contain silver iodide nanocrystals.

Raman spectroscopy and high-energy X-ray diffraction were used to characterise short- and intermediate range ordering of the AgI-HgS-GeS_2 glasses in the composition domains A, B and C. The complementary experimental techniques supported by DFT modelling of the Raman spectra yield consistent structural results: the glass network is essentially formed by corner-sharing CS-$GeS_{4/2}$ tetrahedra and/or CS-Ge_2S_7 dimers. Mercury sulfide in glasses is dimorphic. The majority of Hg species (70 % at $x < 0.2$) are building-up two-fold coordinated $(HgS_{2/2})_n$ chains. The complete disappearance of tetrahedral mercury at $x \gtrsim 0.3$ explains the difference in ionic conductivity between the modifier-controlled sub-regions B and C. Silver species have mixed (2I + 2S) tetrahedral environment forming either edge–sharing ES-$Ag_2I_2S_{4/2}$ dimers or corner-sharing $(CS\text{-}AgI_{2/2}S_{2/2})_n$ chains.

The isolated ES-$Ag_2I_2S_{4/2}$ dimers, randomly distributed in the glass network, presumably exist in the critical percolation domain A, including also the glasses with intermediate conductivity behaviour between the two transport regimes at $x \lesssim 0.1$. The extended $(CS\text{-}AgI_{2/2}S_{2/2})_n$ chains in the modifier-controlled domains B and C are suggested to form preferential conduction pathways ensuring high ionic mobility of Ag^+ cations moving along large polarisable anions. Nevertheless, further AIMD modelling would be necessary to provide further structural and ion dynamics details.

Acknowledgements: This work was partly supported by Agence Nationale de la Recherche (ANR, France) under Grant No. ANR-15-ASTR-0016-01. The work at the Université du Littoral Côte d'Opale was also supported by the Région Hauts de France and the Ministère de l'Enseignement Supérieur et de la Recherche (CPER Climibio) as well as by the European Fund for Regional Economic Development. Work at the Advanced Photon Source, Argonne National Laboratory, was supported in part by the Office of Basic Energy Sciences, U.S. Department of Energy, under Contract No. DE-AC02-06CH1135. The DFT simulations were carried out using the CALCULCO computing platform, supported by SCoSI/ULCO (Service COmmun du Système d'Information de l'Université du Littoral Côte d'Opale).

References

[1] T. Minami, K. Imazawa, M. Tanaka. *J. Non-Cryst. Solids* **42**, 469 (1980).
[2] A. Pradel, M. Ribes. *Chalcogenide Glasses. Preparation, Properties and Applications*, p. 169, Woodhead, Cambridge (2014).
[3] J. Habasaki, C. Leon, K. L. Ngai. *Dynamics of Glassy, Crystalline and Liquid Ionic Conductors*, Springer, Heidelberg (2017).
[4] Yu. G. Vlasov, E. Bychkov. *Ion-Selective Electrode Rev*. **9**, 5 (1987).
[5] M. Milochova, E. Bychkov. *J. Phys. Soc. Jpn., Suppl. A* **79**, 173 (2010).
[6] H. Sakuma, I. Shimizu, H. Kokado, E. Inoue. *Bull. Chem. Soc. Jpn*. **44**, 1723 (1971).
[7] H. Jain, A. Kovalskiy, M. Vlcek. Chalcogenide Glasses. Preparation, Properties and Applications, p. 562, Woodhead, Cambridge (2014).
[8] M. Wuttig, N. Yamada. *Nature Mater*. **6**, 824 (2007).
[9] A. V. Kolobov, J. Tominaga. *Chalcogenides. Metastability and Phase Change Phenomena*, Springer, Heidelberg (2012).
[10] M. Frumar, T. Wagner, K. Shimakawa, B. Frumarova. *Nanomaterials and Nanostructures, NATO Science for Peace and Security Series C: Environmental Security*, p. 151, Springer Science + Business Media, Dordrecht (2015).
[11] J. D. Wicks, L. Börjesson, G. Bushnell-Wye, W. S. Howells, R. L. McGreevy. *Phys. Rev. Lett*. **74**, 726 (1995).
[12] J. Swenson, L. Börjesson. *Phys. Rev. Lett*. **77**, 3569 (1996).
[13] H. W. Sun, B. Tanguy, J. M. Reau, J. J. Videau, J. Portier. *J. Non-Cryst. Solids* **99**, 222 (1988).
[14] E. Bychkov, G. Wortmann. *J. Non-Cryst. Solids* **159**, 162 (1993).
[15] T. Petkova, B. Monchev, O. Kostadinova, P. Petkov, S. N. Yannopoulos. *J. Non-Cryst. Solids* **355**, 2063 (2009).
[16] Y. Onodera, T. Usuki, T. Nasu, S. Kohara. *Solid State Ionics* **262** (2013) 469.

[17] M. Kassem, S. Khaoulani, A. Cuisset, D. Le Coq, P. Masselin, E. Bychkov. *RSC Adv*. **4**, 49236 (2014).
[18] M. Kassem, A. Sokolov, A. Cuisset, T. Usuki, S. Khaoulani, P. Masselin, D. Le Coq, J. C. Neuefeind, M. Feygenson, A. C. Hannon, C. J. Benmore, E. Bychkov. *J. Phys. Chem. B* **120**, 5278 (2016).
[19] R. Zaiter. *Ph.D. thesis*, Université du Littoral Côte d'Opale (2018).
[20] M. Bokova, A. Paraskiva, M. Kassem, I. Alekseev, E. Bychkov. *J. Alloys Compd*. **777**, 902 (2019).
[21] A. P. Hammersley, S. O. Svensson, M. Hanfland, A. N. Fitch, D. Häusermann. *High Pressure Res*. **14**, 235 (1996).
[22] L. B. Skinner, C. J. Benmore, J. B. Parise. *Nucl. Instrum. Methods Phys. Res., Sect. A* **662**, 61 (2012).
[23] *Gaussian 16*, Revision B.01, M. J. Frisch, G. W. Trucks, H. B. Schlegel, G. E. Scuseria, M. A. Robb, J. R. Cheeseman, G. Scalmani, V. Barone, G. A. Petersson, H. Nakatsuji, X. Li, M. Caricato, A. V. Marenich, J. Bloino, B. G. Janesko, R. Gomperts, B. Mennucci, H. P. Hratchian, J. V. Ortiz, A. F. Izmaylov, J. L. Sonnenberg, D. Williams-Young, F. Ding, F. Lipparini, F. Egidi, J. Goings, B. Peng, A. Petrone, T. Henderson, D. Ranasinghe, V. G. Zakrzewski, J. Gao, N. Rega, G. Zheng, W. Liang, M. Hada, M. Ehara, K. Toyota, R. Fukuda, J. Hasegawa, M. Ishida, T. Nakajima, Y. Honda, O. Kitao, H. Nakai, T. Vreven, K. Throssell, J. A. Montgomery, Jr., J. E. Peralta, F. Ogliaro, M. J. Bearpark, J. J. Heyd, E. N. Brothers, K. N. Kudin, V. N. Staroverov, T. A. Keith, R. Kobayashi, J. Normand, K. Raghavachari, A. P. Rendell, J. C. Burant, S. S. Iyengar, J. Tomasi, M. Cossi, J. M. Millam, M. Klene, C. Adamo, R. Cammi, J. W. Ochterski, R. L. Martin, K. Morokuma, O. Farkas, J. B. Foresman, D. J. Fox. Gaussian, Inc., Wallingford CT, 2016.
[24] A. D. Becke. *J. Chem. Phys*. **98**, 5648 (1993).
[25] C. Lee, W. Yang, R. G. Parr. *Phys. Rev. B: Condens. Matter Mater. Phys*. **37**, 785 (1988).
[26] K. A. Peterson, D. Figgen, E. Goll, H. Stoll, M. Dolg. *J. Chem. Phys*. **119**, 11113 (2003).
[27] D. Feller. *J. Comput. Chem*. **17**, 1571 (1996).
[28] E. Bychkov, V. Tsegelnik, Yu. Vlasov, A. Pradel, M. Ribes. *J. Non-Cryst. Solids* **208**, 1 (1996).
[29] Yu. Drugov, V. Tsegelnik, A. Bolotov, Yu. Vlasov, E. Bychkov. *Solid State Ionics* **136–137**, 1091 (2000).
[30] C. Renard, G. Coquet, E. Bychkov. *Solid State Ionics* **154–155**, 749 (2002).
[31] M. Kassem, S. Khaoulani, E. Bychkov. *J. Am. Ceram. Soc*. **101**, 2287 (2018).
[32] E. Bychkov. *Solid State Ionics* **180**, 510 (2009).
[33] E. Bychkov, D. L. Price, A. Lapp. *J. Non-Cryst. Solids* **293–295**, 211 (2001).
[34] E. Bychkov, D. L. Price, C. J. Benmore, A. C. Hannon. *Solid State Ionics* **154–155**, 349 (2002).
[35] E. Bychkov, Yu. Tveryanovich, Yu. Vlasov. *Semiconducting Chalcogenide Glasses III, Applications of Chalcogenide Glasses*, p. 103, Elsevier, New York (2004).
[36] R. Zallen, G. Lucovsky, W. Taylor, A. Pinczuk, E. Burstein. *Phys. Rev. B: Condens. Matter Mater. Phys*. **1**, 4058 (1970).
[37] W. Imaino, C. T. Simpson, W. M. Becker, A. K. Ramdas. *Phys. Rev. B: Condens. Matter Mater. Phys*. **21**, 634 (1980).
[38] P. Masselin, D. Le Coq, A. Cuisset, E. Bychkov. *Opt. Mater. Express* **2**, 1768 (2012).
[39] A. Paraskiva. *Ph.D. thesis*, Université du Littoral Côte d'Opale (2017).
[40] A. J. Frueh. *Z. Kristallogr*. **110**, 136 (1958).
[41] C. Rau, P. Armand, A. Pradel, C. P. E. Varsamis, E. I. Kamitsos, D. Granier, A. Ibanez, E. Philippot. *Phys. Rev. B: Condens. Matter Mater. Phys*. **63**, 184204 (2001).
[42] S. C. Rowland, S. Narasimhan, A. Bienenstock. *J. Appl. Phys*. **42**, 2741 (1972).
[43] I. Petri, P. S. Salmon. *J. Non-Cryst. Solids* **293–295**, 169 (2001).
[44] E. Bychkov, M. Miloshova, D. L. Price, C. J. Benmore, A. Lorriaux. *J. Non-Cryst. Solids* **353**, 63 (2006).
[45] A. Bytchkov, G. J. Cuello, S. Kohara, C. J. Benmore, D. L. Price, E. Bychkov. *Phys. Chem. Chem. Phys*. **15**, 8487 (2013).
[46] J. Akola, A. Sokolov, E. Bychkov. *CNRS Spring School on Glass Structure*, Cargèse, France, March 27–31, (2017).
[47] J. Akola, B. Beuneu, R. O. Jones, P. Jóvári, I. Kaban, J. Kolář, I. Voleská, T. Wágner. *J. Phys.: Condens. Matter* **27**, 485304 (2015).
[48] A. Zeidler, J. W. E. Drewitt, P. S. Salmon, A. C. Barnes, W. A. Crichton, S. Klotz, H. E. Fischer, C. J. Benmore, S. Ramos, A. C. Hannon. *J. Phys.: Condens. Matter* **21**, 474217 (2009).
[49] E. Lorch. *J. Phys. C: Solid State Phys*. **2**, 229 (1969).
[50] S. Le Roux, P. Jund. *Comput. Mater. Sci*. **49**, 70 (2010).
[51] K. Itoh. *J. Phys. Chem. Solids* **103**, 109 (2017).
[52] T. Schleid, P. Lauxmann, C. Schneck. *Z. Kristallogr*. **16**, 95 (1999).
[53] D. Rodic, V. Spasojevic, A. Bajorek, P. Onnerud. *J. Magn. Magn. Mater*. **152**, 159, (1996).
[54] F. Schnieders, P. Böttcher. *Z. Kristallogr*. **210**, 323 (1995).
[55] T. Nilges, S. Reiser, J. H. Hong, E. Gaudin, A. Pfitzner. *Phys. Chem. Chem. Phys*. **4**, 5888 (2002).
[56] H. J. Deiseroth, M. Wagener, E. Neumann. *Eur. J. Inorg. Chem*. **2004**, 4755 (2004).
[57] C. Näther, A. Beck. *Z. Naturforsch. B* **59**, 992 (2004).
[58] A. Beck, C. Näther. Z. *Naturforsch. B* **61**, 517 (2006).
[59] H.-L. Keller, L. Wimbert. *Z. Anorg. Allg. Chem*. **629**, 2337 (2003).
[60] J. Beck, H.-L. Keller, M. Rompel, L. Wimbert, B. Ewald, *Z. Anorg. Allg. Chem*. **630**, 1031 (2004).